In-situ U-Pb geochronology and sulfur isotopes constrain the metallogenesis of the giant Neves Corvo deposit, Iberian Pyrite Belt

Xiang Li[a], Kui-Dong Zhao[a,*], Shao-Yong Jiang[a], Martin R. Palmer[b]

[a] *State Key Laboratory of Geological Processes and Mineral Resources, Collaborative Innovation Center for Exploration of Strategic Mineral Resources, Faculty of Earth Resources, China University of Geosciences, Wuhan 430074, PR China*
[b] *National Oceanography Centre, School of Ocean and Earth Science, University of Southampton, Southampton SO14 3ZH, UK*

ABSTRACT

The large-scale, high-grade Sn ores and the Cu-Sn metal association in the volcanic massive sulfide (VMS) ores in Neves Corvo are unique among VMS deposits, not only in the Iberian Pyrite Belt but also worldwide. Thus, the exceptional nature of the Neves Corvo deposit calls for unusual metallogenic processes. Previous efforts to constrain these processes have been hampered by a lack of high precision ages for the mineralization. This has led to a debate as to whether tin mineralization occurred at the same time as the associated volcanism and VMS-style mineralization, or is the result of later processes events associated with the Hercynian orogeny. We report *in-situ* U-Pb dating results of hydrothermal cassiterite and sulfur isotopic compositions of sulfides in the Neves Corvo deposit that place tight constraints on the timing of mineralization and on the origin of the hydrothermal ore-forming fluids. The cassiterite samples yield U-Pb ages of the Sn mineralization of 363–366 Ma; identical to the age of the host volcanic rocks. $\delta^{34}S$ values range from $-32.3‰$ to $+17.4‰$ among the different VMS ore types and are largely consistent with microbiological reduction of seawater sulfate, but with some positive values resulting from thermochemical sulfate reduction. In contrast, the Sn-rich ores have a limited range in $\delta^{34}S$ that clusters near 0‰, which suggests derivation from magmatic fluids. Hence, the unusually high Sn grades at the Neves Corvo deposit are interpreted to be derived from fluids exsolved from a hidden granitic source essentially synchronous with formation of the volcanic rocks and VMS mineralization.

1. Introduction

Most major Sn deposits are spatially and chemically associated with highly differentiated, low oxygen fugacity granitic rocks (Heinrich, 1990; Lehmann, 1990; Taylor and Wall, 1992) and significant tin mineralization rarely occurs in typical volcanic massive sulfide (VMS) deposits. In contrast, the Neves Corvo VMS deposit that formed in a submarine hydrothermal setting, has large-scale and high-grade Sn mineralization (Relvas et al., 2006a). The Neves Corvo deposit is located in the Portuguese part of the Iberian Pyrite Belt (IPB), the largest metallogenic province of VMS deposits in the world (Fig. 1). In addition to being one of the largest Cu deposits (the initial resource was 34 Mt @ 8.5% Cu) in Europe, it is remarkable because of its high Sn grades (up to 60% SnO_2) (Carvalho et al., 2018). The geology and origin of the Neves Corvo deposit has been extensively studied (e.g. Relvas et al., 2001, 2006a,b; Moura, 2005, 2008; Munhá et al., 2005). Nevertheless, the exact timing of the Sn mineralization and the origin of the Sn-bearing ore fluids are not fully understood. Modified seawater has been

interpreted as the main fluid involved in most IPB systems (Inverno et al., 2008; Tornos et al., 2008), but the remarkable anomaly of mineralization has been suggested to result from the addition of magmatic (Huston et al., 2011; Relvas et al., 2001, 2006a,b) or metamorphic fluids (Moura, 2008) to the hydrothermal system of Neves Corvo. However, previous Rb-Sr (Relvas et al., 2001) and Re-Os (Munhá et al., 2005) isotope studies of the sulfide ores contain uncertainties that are too large to determine whether the ores formed during the main IPB mineralization or during a later metamorphic event, such as the Hercynian orogeny.

The high concentrations of lattice-bound U in cassiterite and its high closure temperature (> 500 °C and up to 900 °C) for U-Pb isotopes (Gulson and Jones, 1992), has led to cassiterite being recognized as a robust U-Pb geochronometer for direct dating of Sn mineralization events (Yuan et al., 2008; Zhang et al., 2017). In addition, *in-situ* sulfur isotopic analyses of the fine-grained and complex ore minerals can reveal important information about the nature of sulfide precipitation and the origin of the hydrothermal fluids. Here, we present new *in-situ* U-Pb
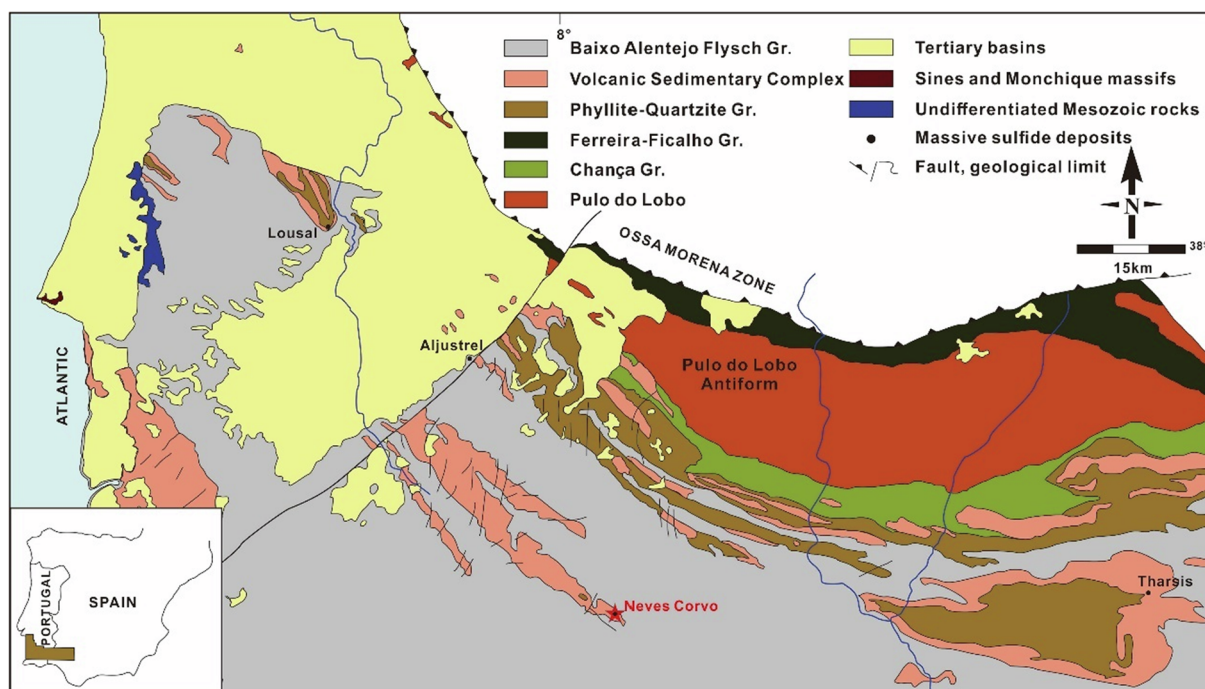
Fig. 1. Geological map of the South Portuguese Zone, including the Iberian Pyrite Belt and associated VMS deposits, showing location of the Neves Corvo deposit area (after Inverno et al., 2015).

dating results of cassiterite and sulfur isotopic data from the Neves Corvo deposit in an attempt to constrain the mineralization age and the origin of the ore-forming fluids.

2. Geology of the Neves Corvo deposit

2.1. Deposit geology

The IPB is thought to have formed in a series of marine basins opened in response to faulting generated during collision between the South Portuguese Zone and the Iberian terranes during the Devonian-Carboniferous (Oliveira et al., 2004; Tornos et al., 2005). Local extensional conditions in an overall transpressive regime triggered felsic and mafic volcanism and the associated submarine hydrothermal activity responsible for the VMS deposits. The Neves Corvo deposit contains seven known massive and stringer sulfide orebodies (the Neves, Corvo, Graça, Lombador, Zambujal, Semblana and Monte Branco, Fig. 2) that lie at the southeastern termination of the Rosário-Neves Corvo anticline in the Portuguese segment of the IPB. Excluding the stockwork zones, these orebodies contain 369 Mt of massive sulfide mineralization, of which 198 Mt are massive sulfide ores @ 2.10% Cu, 4.28% Zn, 0.92% Pb, 0.13% Sn, 59.13 ppm Ag and 0.47 ppm Au (Carvalho et al., 2018). The orebodies are located at sub-surface depths of 230 m to ~1000 m. The main massive lenses are hosted by dark shale (Fig. 3) and lie above a sulfide stockwork located in the footwall of felsic Volcanic Sedimentary Complex (VSC), which comprises the products of explosive and effusive rhyolitic eruptions intercalated with mudstone. The VSC can be further subdivided into three volcanic sequences spanning ~30 Ma from late Famennian to mid-late Visean (Rosa et al., 2008). This complex is capped by the Baixo Alentejo Flysch Group; consisting of shale, litharenite and rare conglomerate. Most orebodies at Neves Corvo enclose several stacked ore lenses whose spatial distribution is thought to have been controlled by the paleogeomorphology of the basin (Relvas et al., 2006a). Intense structural deformation and prehnite-pumpellyite-lower greenschist facies metamorphism also affected the deposits during the Hercynian orogeny (Munhá, 1990).

2.2. Mineralization and alteration

Three main ore types were classified on the basis of the sulfide stratigraphy, and each type has been further subdivided according to their chemical composition; e.g., their Cu, Zn, Pb, Ag and Sn grades (Gaspar, 2002): (1) fissural ore (with copper-rich stringer ore (FC, Fig. 4A), cassiterite-rich stringer ore (FT, Fig. 4B) and zinc-rich stringer ore (FZ)), which is a typical stockwork mineralization hosted by felsic volcanic and volcaniclastic rocks in the footwall sequence, (2) massive sulfide ore (copper-rich massive sulfide ores (MC, Fig. 4C), high copper and tin massive sulfide ores (MS, Fig. 4D), massive cassiterite ores (MT, Fig. 4E), high copper and zinc massive sulfide ores (MCZ), high zinc and lead massive sulfide ores (MZP), lead-rich massive sulfide ores (MP) and zinc-rich massive sulfide ores (MZ, Fig. 4F)), which is the most abundant ore type, and (3) rubané ore, which include copper-rich banded ore in a hanging wall position (RC, Fig. 4G) and cassiterite-rich banded ore in a hanging wall position (RT, Fig. 4H), described as a highly deformed and ribbon-like type of mineralization interpreted as remobilized parts of the primitive stockwork tectonically transported to the top of the massive sulfides (Relvas et al., 2006a). The sub-economic barren massive sulfides (ME) are generally located in the upper part of the orebodies.

Most primary textures and textural relationships between the sulfide ore minerals are obscured either by hydrothermal re-working processes, and/or by late-Hercynian tectonic metamorphic overprinting effects. The sulfide minerals are usually dominated by pyrite, with large (locally dominant) amounts of chalcopyrite, sphalerite and galena. Accessory and trace mineral assemblages include stannite, arsenopyrite, tetrahedrite, tennantite, kesterite, ferrokesterite, boulangerite, pyrrhotite, cobaltite, cosalite and native bismuth (Gaspar, 2002; Relvas et al., 2006a,b; Carvalho et al., 2018). Chalcopyrite contains abundant sphalerite inclusions (chalcopyrite disease, Fig. 4D). Cellular and zoned botryoidal (colloform) pyrite textures observed in the present study are shown in Fig. 4D. Sulfates are lacking in the mineral assemblage of all types of ores.

In contrast to most IPB deposits, the Neves Corvo deposit is enriched in Sn. Although accessory cassiterite is present in some IPB deposits
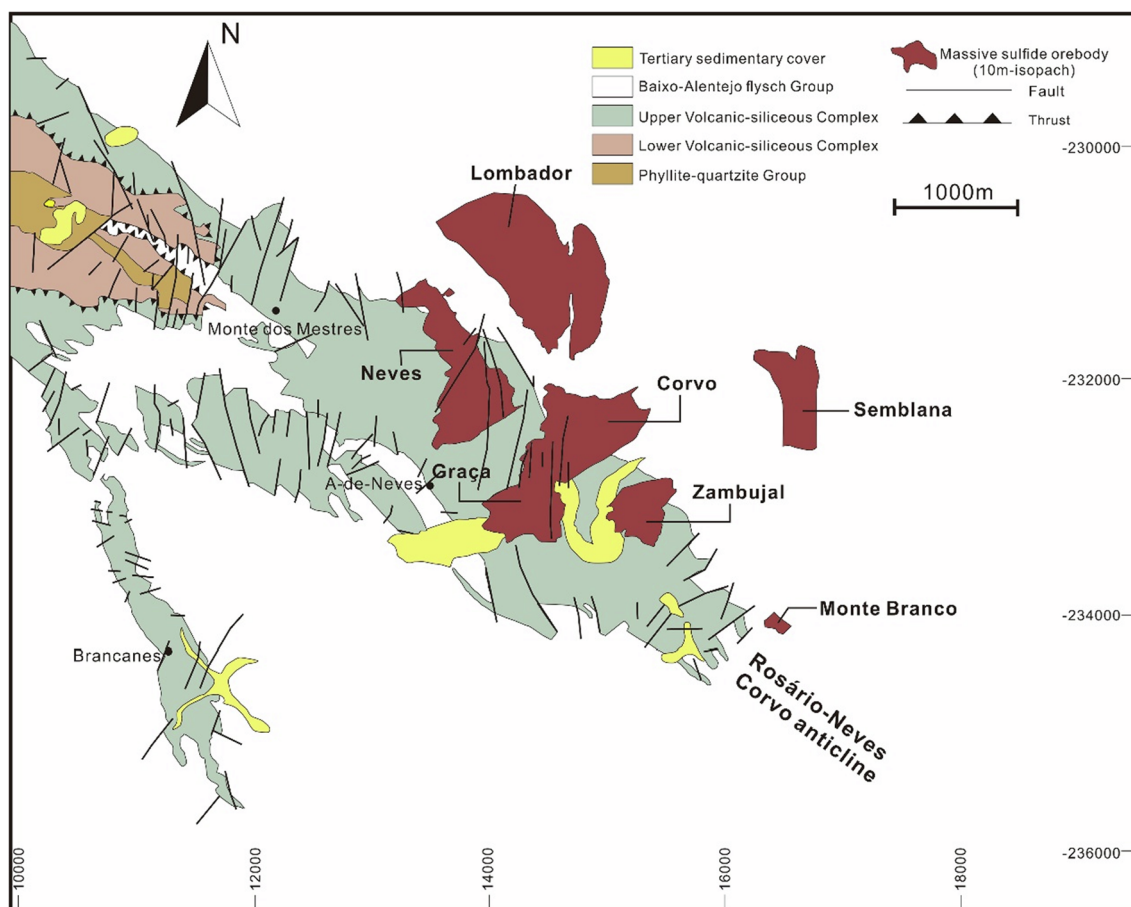
Fig. 2. Geologic map of the Rosário-Neves Corvo anticline. The projection on surface of the massive sulphide ore 10-m isopach contour indicates location of the seven Neves-Corvo orebodies (modified after Relvas et al., 2006a).

(Marcoux et al., 1996; Tornos et al., 2008; Inverno et al., 2008), the cassiterite in these deposits generally occurs as very small inclusions in sulfide. Cassiterite as an inclusion in sulfide has not been found in the Neves Corvo deposit. Rather, most of the tin occurs as relatively low-grade disseminated cassiterite associated with Cu-rich ore and the remainder occurs as massive and stringer cassiterite. The stringer and massive cassiterite mineralization is mostly present within the so-called "tin corridor" (Relvas et al., 2006a), which is a north-south structural alignment interpreted as corresponding to a paleochannel bound by syn-volcanic faults. The cassiterite commonly occurs as fine-grained aggregates of subeuhedral to euhedral prismatic crystals that generally show fracturing (Fig. 5E, F). Some larger cassiterite clasts are enclosed in a mass of chalcopyrite, sphalerite and very fine grained cassiterite (Fig. 5B). The cassiterite aggregates in the FT ores are commonly intergrown with pyrite and quartz.

The footwall hydrothermal alteration zonation recognized at the Neves Corvo deposit comprises an inner chlorite/donbassite-quartz-sulfide-(sericite) core that grades outward into successive enveloping K-sericite-quartz-sulfide and Na-sericite-quartz-sulfide halos (Relvas et al., 2006a). The alteration mineralogy, geochemistry and stable isotopes indicate that ore fluids at the Neves Corvo deposit were hotter and more acidic than typical IPB ore forming fluids (Relvas et al., 2006a,b)

3. Sampling and analytical methods

The study of cassiterite U–Pb dating and sulfur isotope analysis in the Neves Corvo deposit was based on a targeted sampling strategy at the Corvo orebody. The ore types considered in this study follow the

categories defined in the mine, which include stockwork ores (FT and FC), massive sulfide ores (MC, MT, MZ and MS), rubané ores (RT and RC) and barren massive sulfides (ME). Four samples from three different ore types, fissural (NC-14), massive sulfide (NC-4) and rubané ores (NC-5a, NC-5b) were chosen to determine the timing of mineralization, and 14 samples from 9 ore subtypes (FT, FC, MC, MS, MT, MZ, RC, RT, ME) were analyzed for sulfur isotope compositions of the sulfides. *In-situ* U-Pb dating was carried out by laser ablation inductively coupled plasma mass spectrometry (LA-ICP-MS) system. *In-situ* sulfur isotope analysis was carried out using a multi-collector inductively coupled plasma mass spectrometer (MC-ICP-MS) system, equipped with a 193 nm ArF excimer laser.

3.1. Cassiterite U-Pb dating analysis

Mineral assemblages were studied in fourteen polished sections using a standard petrographic microscope and the cassiterite grains selected for dating were checked under the back-scattered electron (BSE) imaging to ensure that they were free of mineral inclusions and cracks. The microphotographs and BSE images were taken at the State Key Laboratory of Geological Processes and Mineral Resources (GPMR), China University of Geosciences, Wuhan.

The *in-situ* U-Pb dating of cassiterite was carried out by LA-ICP-MS in the GPMR. The system consists of a Thermal iCAP Qc ICP-MS coupled with a RESOlution S-155 193 nm ArF excimer laser. Helium gas carrying the ablated sample aerosol was mixed with argon carrier gas and nitrogen as an additional diatomic gas to enhance sensitivity, before flowing into the ICP-MS. Prior to analysis, the LA-ICP-MS system was optimized using NIST SRM 612 ablated with a 50 μm spot size and
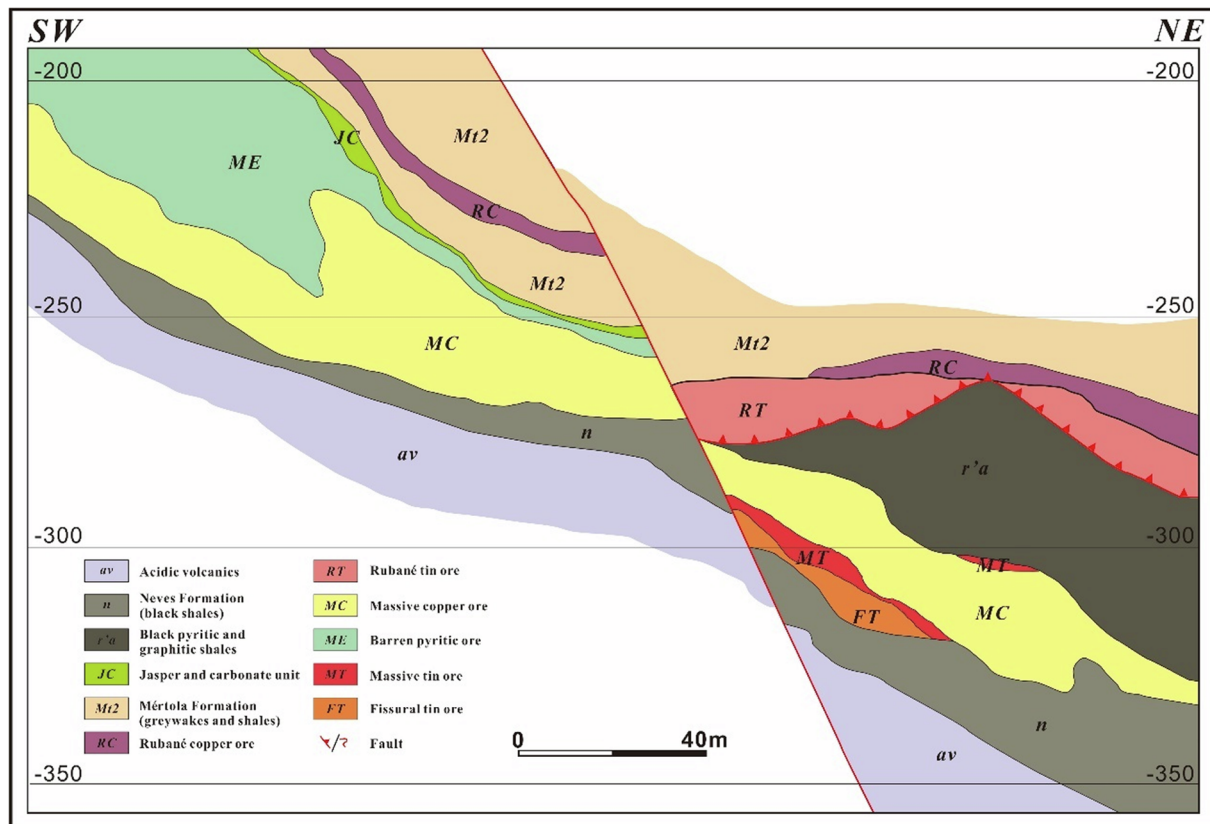
Fig. 3. Cross-section of the Corvo orebody showing the distribution of the various tin ores in relation to the copper-rich ores at its northeastern extremity (after Cabri et al., 1998).

5 μm/s scan speed to achieve maximum signal intensity and low oxide rate. NIST SRM 612 and an in-lab cassiterite standard AY-4 were used as an external elemental and isotopic calibration standard. AY-4 was collected from the No. 19 skarn orebody in the Anyuan tin deposit of the Furong orefield in Hunan Province, South China. The U-Pb age of the standard cassiterite (AY-4) was established by ID-TIMS as 158.2 ± 0.4 Ma (Yuan et al., 2011). It also has very low common lead. Each set of 10 analyses was followed by two measurements of AY-4 and one measurement of NIST SRM 612. Based on the reflected light photomicrographs and BSE images, the laser was focused to produce an ablation pit with a diameter of 50 μm, and a laser pulse rate of 8 Hz with an energy density of approximately 3–4 J/cm^2. Each spot analysis consisted of a 30 s background acquisition and 40 s data acquisition, and 60 s for cleaning the sample cell and plumbing lines. The isotopes were measured in time-resolved mode. For U-Pb dating, dwell times for each mass scan are 20 ms for ^{238}U, ^{232}Th, ^{208}Pb, ^{206}Pb, ^{204}Pb and 40 ms for ^{207}Pb. Concordia diagrams and ^{206}Pb/^{238}U weighted mean calculations of cassiterite were made using Isoplot 4.0 (Ludwig, 2012). Data errors for isotopic ratios in the cassiterite samples are 2σ. The measured, uncorrected compositions of cassiterites were plotted on a Tera-Wasserburg Concordia diagram (Tera and Wasserburg, 1972), and they define a line that intersects the y-axis at the common ^{207}Pb/^{206}Pb value and shows a lower intercept age, approximately representing the sample formation age. The measured ^{207}Pb was corrected for common-Pb using the two-stage model of Stacey and Kramers (1975).

3.2. Sulfur isotope analysis

Sulfur isotope analyse were carried out on sulfides from standard polished sections using a Nu Plasma II multi-collector inductively coupled plasma mass spectrometer (MC-ICP-MS) system, equipped with a RESOlution S-155 193 nm ArF excimer laser at the GPMR, China University of Geosciences, Wuhan. During the experiment, the diameter of the laser spot was 33 μm with a laser repetition rate of 10 Hz, and the ablation process was set to last for 40 s. Standard sample bracketing (SSB) was used to determine the δ^{34}S values of the samples throughout the MC-ICP-MS analytical sessions. An international sphalerite standard NBS-123 (δ^{34}S$_{V-CDT}$ = +17.1‰) and an in-house pyrite standard named WS-1, consisting of a natural pyrite crystal from the Wenshan polymetallic skarn deposit in Yunnan Province in South China, was used to calibrate the mass bias for S isotopes. The δ^{34}S$_{V-CDT}$ values (+1.1‰ ± 0.2‰) of WS-1 were determined with SIMS at the Chinese Academy of Geochemistry, Guangzhou (Zhu et al., 2016). The true sulfur isotope ratio of un-known samples was calculated by correction for instrumental mass bias by linear interpolation between the biases calculated from two neighboring standard analyses. The 2σ analytical precision was about ± 0.3 per mil.

4. Results

4.1. Cassiterite U-Pb dating

The cassiterite consists of euhedral to subhedral crystals, ranging from 10 to 800 μm in diameter, or as clusters of finer grains. The U-Pb dating results of cassiterite are summarized in Table 1 and illustrated in Fig. 6. The U-Pb isotope data define well-constrained lines on the Tera-Wasserburg (TW) diagrams for each sample. Cassiterite from the fissural ores and the massive ores yield TW U-Pb intercept ages of 367.5 ± 8.7 Ma (n = 34, MSWD = 0.98) and 364.4 ± 4.4 Ma (n = 40, MSWD = 0.7), respectively. Two samples from the rubané ore, yield TW U-Pb intercept ages of 365.2 ± 5.3 Ma (n = 34, MSWD = 0.84) and 363.4 ± 5.8 Ma (n = 38, MSWD = 0.9). Using the ^{207}Pb correction method, the weighted mean ^{206}Pb/^{238}U age agrees well with the lower intercept age for each sample. We therefore
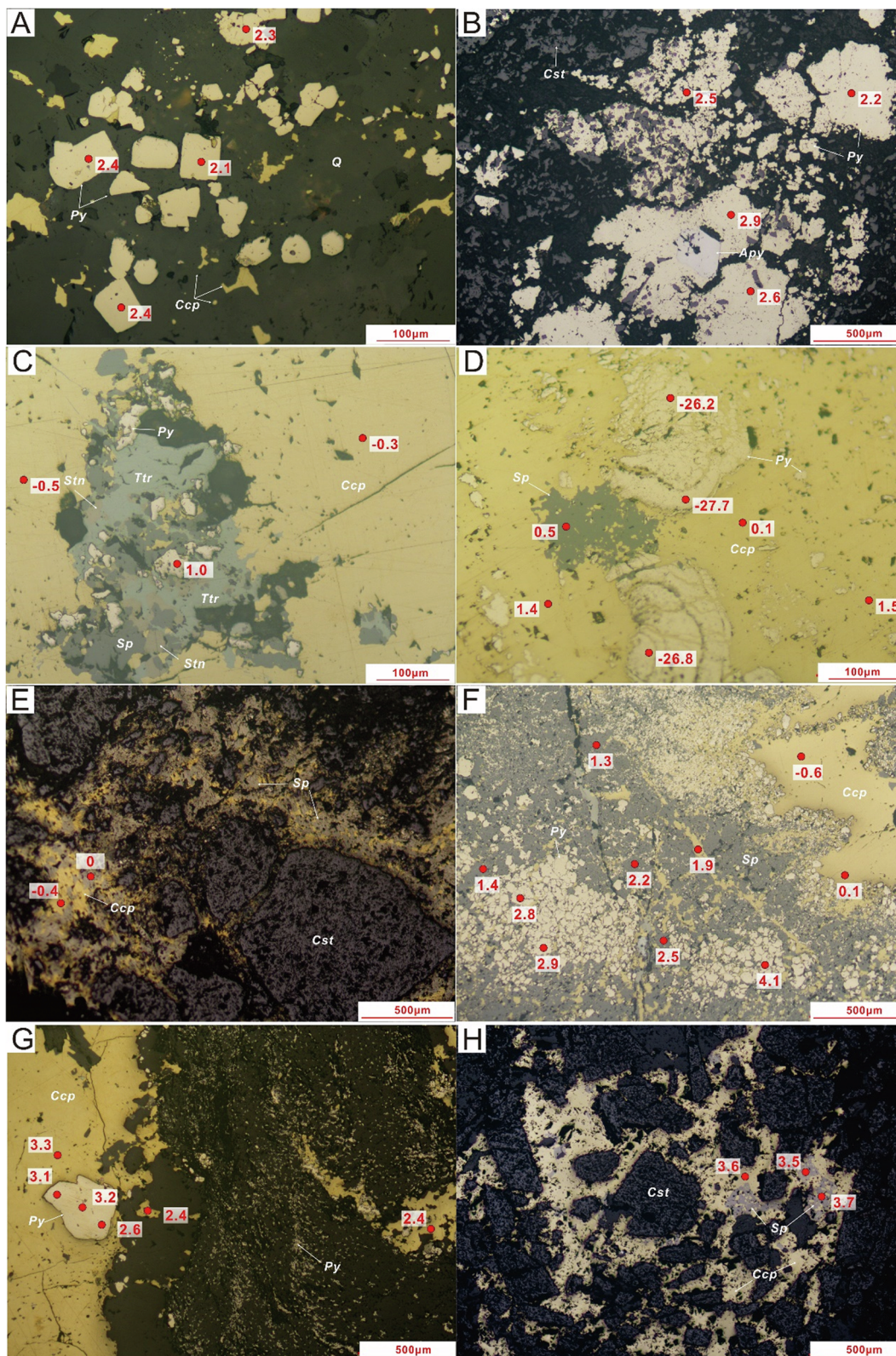
Fig. 4. Photomicrographs of Neves Corvo sulfide textures and sulfur isotope analysis locations and results. A: Sample NC-7a from copper-rich stringer ore (FC). Fine-grained euhedral to subhedral crystals of pyrite intergrown with chalcopyrite. B: Sample NC-14 from fissural stanniferous ore (FT). C: Sample NC-1 from copper-rich massive sulfide ore (MC). Subhedral crystals of pyrite intergrown with sphalerite, tetrahedrite and stannite in chalcopyrite matrix. D: Sample NC-6 from high copper and tin massive sulfide ore (MS), with fragment of pyrite with colloform texture in chalcopyrite matrix. Coarse-grained sphalerite shows the chalcopyrite disease texture. E: Sample NC-4 from massive cassiterite ore (MT), sphalerite intergrown with chalcopyrite. F: Sample NC-12 from zinc-rich massive sulfide ore (MZ). Owing to late tectonic-metamorphic overprinting effects, fractured pyrite is commonly observed. G: Sample NC-10 from rubané cupriferous ore (RC). Late, post-metallo-genetic and tectonic-metamorphic-related generation of pyrite and quartz veinlet crosscutting chalcopyrite. H: Sample NC-5a from rubané stanniferous ore (RT). The euhedral to subhedral crystals of cassiterite occur intergrown with chalcopyrite and sphalerite. Abbreviations: Cst-cassiterite, Py-pyrite, Ccp-chalcopyrite, Sp-sphalerite, Ttr-tetrahedrite, Stn-stannite.
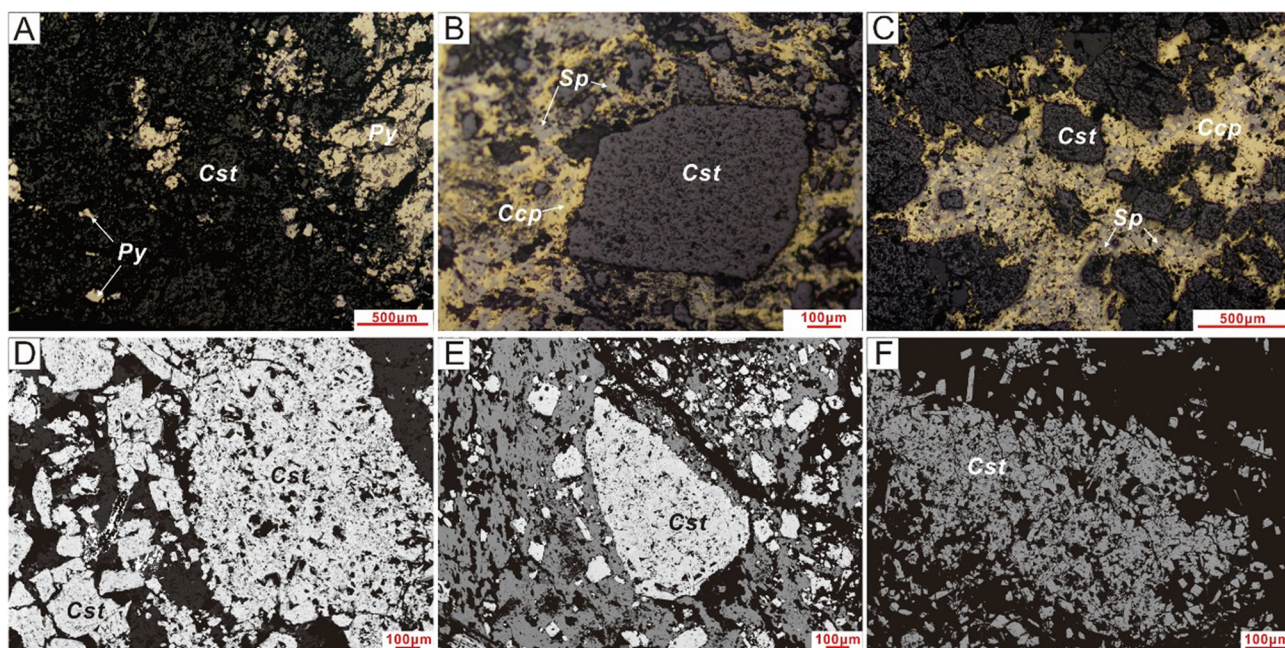
Fig. 5. Photomicrographs (A–C) and BSE images (F–K) showing the occurrences of cassiterite investigated in this study. A, D: Sample NC-14 from fissural cassiterite ore (FT). The cassiterite occurs as fine-grained aggregates of subeuhedral to euhedral prismatic crystals. B, E: Sample NC-4 from massive cassiterite ore (MT). The cassiterite crystals are subeuhedral to euhedral and generally show fracturing. The larger cassiterite clast is enclosed in a mass of chalcopyrite, sphalerite and very fine grained cassiterite. C, F: Sample NC-5a from rubané cassiterite ore (RT). Abbreviations: Cst-cassiterite, Py-pyrite, Ccp-chalcopyrite, Sp-sphalerite.

interpret the cassiterite crystallization age, i.e., the timing of the Sn mineralization event in the Neves Corvo deposit as 363–366 Ma.

4.2. Sulfur isotope data

Over 350 sulfur isotope compositions of sulfides (213 pyrite, 114 chalcopyrite, 41 sphalerite) were determined in 14 samples from 9 ore subtypes. The sulfur isotopic analyses are listed in Table 2 and plotted in Fig. 7.

The $\delta^{34}S$ values of the sulfides range from $-32.3‰$ to $+17.4‰$ and consistent differences exist between the different ore types. The data from the fissural ores range between $-0.5‰$ and $+12.5‰$ with a mean of $+2.9‰$ and one value is $< 0‰$. Sulfides from the massive sulfide ores (especially in the cupriferous ores) show a wide range of $\delta^{34}S$ values (MC: $-12.8‰$ to $+7.1‰$ mean $-3.9‰$, MS: $-32.3‰$ to $+17.4‰$ mean $-5.0‰$). The most negative $\delta^{34}S$ values in the massive ore body are associated with the colloform-texture pyrite and associated minerals (Fig. 4). Similarly negative values have been observed in framboidal and other early pyrites at Aznalcóllar, Tharsis, and Concepción in the eastern IPB (Velasco et al., 1998). The $\delta^{34}S$ values from the massive stanniferous ore and massive Zn-rich ore have relatively homogeneous values (MT: $-0.9‰$ to $+1.5‰$ mean $0.1‰$, MZ: $-0.6‰$ to $+4.1‰$ mean $+1.7‰$). Sulfide minerals from the rubané ores display positive values between $+1.7‰$ and $+4.8‰$ and a mean of $+2.9‰$. The similarity in $\delta^{34}S$ values between the rubané and fissural ores is compatible with the hypothesis that the rubané ores were remobilized from the primitive stockwork (Gaspar, 2002). In comparison, the barren massive sulfide ores have heavier values of $+2.5‰$ to $+9.9‰$ with a mean of $+6.0‰$. It is noteworthy that the Sn-rich ores are close to $0‰$ and show limited $\delta^{34}S$ variation (FT: $+0.7‰$ to $+3.1‰$, MT: $-0.9‰$ to $+1.5‰$, RT: $1.7‰$ to $+4.8‰$).

5. Discussion

5.1. Timing of tin mineralization

Rb-Sr and Re-Os geochronological studies of the sulfide ores have

constrained ore formation of the Neves Corvo deposit to $347 \pm 25\,Ma$ (Relvas et al., 2001) and $358 \pm 29\,Ma$ (Munhá et al., 2005), respectively. For other deposits in the IPB, available formation ages based on Re-Os isotopes from the Tharsis and Río Tinto sulfides are $353 \pm 44\,Ma$ and $346 \pm 26\,Ma$ respectively (Mathur et al., 1999). These relatively large errors may be caused by heterogeneity within the hydrothermal system (long-lived hydrothermal event and multiple volcanic episodes of overprinting), or subsequent disturbance of the isotopic system associated with hydrothermal alteration and thermal events during the Hercynian orogeny (330–300 Ma) (Munhá, 1990). The coincidence of the timing of the Hercynian orogeny within the errors of the Rb-Sr and Re-Os ages has led to the suggestion that some of the ores were formed by metamorphic-derived fluids during orogenic metamorphism (Moura, 2008).

Recent U-Pb dating of zircons from felsic rocks in the Rosário-Neves Corvo anticline area indicates five episodes of felsic volcanism at 384, 373, 365, 359 and 354 Ma, respectively (Oliveira et al., 2013). Thus high heat flow was maintained in the region for ~30 Myr and may have had an important role in the formation of the deposit. Importantly, these ages overlap within uncertainty with the dates we obtained for the Neves Corvo cassiterite mineralization at 363–366 Ma. This observation confirms that the Sn ores were not formed from metamorphic fluids during the later Hercynian orogeny, but rather were temporally coincident with the submarine hydrothermal system generated during the felsic volcanism, which corroborates the conclusions from previous studies (e.g. Relvas et al., 2001, 2006a,b; Gaspar, 2002; Huston et al., 2011).

5.2. Sulfur sources

Large numbers of studies of modern and ancient VMS deposits indicate that the three main sources of sulfur in these deposits are: (1) sulfur leached from igneous footwall rocks and/or direct contributions from magmatic fluids with $\delta^{34}S \approx -5$ to $+5‰$ (averaging $0‰$); (2) seawater sulfate that is present in sulfate minerals or is reduced by thermochemical processes; (3) sedimentary or dissolved sulfur derived from the microbiological reduction of marine sulfate.

Table 1
LA-ICPMS U-Pb dating results for cassiterite from the Neves Corvo deposit.

Spots	Isotopic ratios						Ages(Ma)		^{207}Pb-Corrected ages(Ma)	
	^{207}Pb/^{206}Pb	2σ	^{207}Pb/^{235}U	2σ	^{206}Pb/^{238}U	2σ	^{206}Pb/^{238}U	2σ	^{206}Pb/^{238}U	2σ
NC-14–1	0.49424	0.01090	8.62684	0.23082	0.12660	0.00246	767.8	14.9	362.7	13.0
NC-14-2	0.48364	0.00851	8.69604	0.16858	0.13041	0.00165	789.8	10.0	383.7	12.5
NC-14-3	0.43474	0.01136	6.77785	0.18936	0.11308	0.00198	690.4	12.1	375.6	13.0
NC-14-4	0.39481	0.00576	5.38809	0.08138	0.09898	0.00089	608.5	5.5	359.7	11.3
NC-14-5	0.68794	0.01146	27.07461	1.21304	0.28544	0.01216	1619.1	69.0	390.0	20.3
NC-14-6	0.62482	0.01197	18.00368	0.80582	0.20898	0.00874	1223.9	51.2	387.3	19.9
NC-14-7	0.55228	0.01349	11.39932	0.36598	0.14970	0.00372	899.8	22.3	361.9	14.1
NC-14-8	0.44295	0.00969	7.01638	0.16915	0.11488	0.00181	701.6	11.1	374.3	12.7
NC-14-9	0.42188	0.00879	6.22843	0.14280	0.10708	0.00160	657.9	9.8	366.5	12.3
NC-14-10	0.68900	0.01110	25.26333	0.76961	0.26594	0.00727	1524.0	41.5	361.9	14.7
NC-14-11	0.35711	0.01282	4.71419	0.18333	0.09574	0.00237	590.7	14.6	375.4	14.6
NC-14-12	0.44812	0.01476	7.01181	0.27078	0.11349	0.00308	694.0	18.8	365.5	14.8
NC-14-13	0.27636	0.00783	3.14000	0.08452	0.08240	0.00106	510.9	6.6	374.4	12.2
NC-14-14	0.30747	0.01936	3.81616	0.24643	0.09002	0.00337	555.8	20.8	387.1	18.6
NC-14-15	0.46085	0.01183	7.13250	0.21060	0.11225	0.00228	684.8	13.9	350.9	12.7
NC-14-16	0.50611	0.01253	9.04646	0.23728	0.12964	0.00209	784.2	12.7	359.7	12.3
NC-14-17	0.32806	0.00894	4.13148	0.09414	0.09134	0.00126	575.2	7.8	378.5	12.5
NC-14-18	0.75357	0.00773	43.03715	1.35859	0.41421	0.01277	2267.8	68.7	357.3	15.4
NC-14-19	0.69153	0.01779	24.00885	0.74840	0.25181	0.00656	1465.8	37.7	338.4	13.4
NC-14-20	0.57508	0.01542	13.17580	0.35297	0.16617	0.00332	1000.1	19.8	372.1	13.4
NC-14-21	0.47517	0.01203	7.77578	0.17406	0.11869	0.00175	727.1	10.7	357.7	12.0
NC-14-22	0.42554	0.01328	6.27084	0.20684	0.10688	0.00274	655.8	16.8	362.9	14.3
NC-14-23	0.49143	0.01371	8.65869	0.27473	0.12779	0.00329	770.9	20.0	368.7	14.6
NC-14-24	0.59574	0.01972	14.99414	0.50351	0.18255	0.00463	1071.0	27.4	379.4	14.9
NC-14-25	0.57283	0.01390	12.13424	0.31573	0.15364	0.00314	909.4	18.8	347.4	12.6
NC-14-26	0.42979	0.01490	6.59178	0.20609	0.11124	0.00235	668.4	14.4	373.8	13.7
NC-14-27	0.54149	0.01716	10.58614	0.29610	0.14179	0.00258	847.9	15.6	354.8	12.4
NC-14-28	0.52924	0.01414	9.94509	0.24179	0.13629	0.00224	818.9	13.5	353.9	12.1
NC-14-29	0.59390	0.01776	14.41201	0.55783	0.17600	0.00583	1041.5	34.6	368.6	16.5
NC-14-30	0.66401	0.01635	22.00803	0.54632	0.24039	0.00446	1387.2	25.8	373.2	13.2
NC-14-31	0.43303	0.01255	6.30808	0.16000	0.10565	0.00172	648.2	10.6	352.9	12.1
NC-14-32	0.45075	0.01435	6.93680	0.20175	0.11162	0.00221	684.5	13.5	357.5	12.8
NC-14-33	0.66146	0.01390	22.63179	0.85149	0.24815	0.00866	1436.8	49.8	389.7	17.9
NC-14-34	0.57599	0.01464	13.48426	0.45367	0.16979	0.00493	1019.0	29.3	378.8	15.8
NC-4-1	0.17629	0.00693	1.62113	0.06048	0.06670	0.00107	412.5	6.7	355.5	12.1
NC-4-2	0.10606	0.00511	0.91218	0.04010	0.06238	0.00095	387.2	6.0	365.8	12.3
NC-4-3	0.13179	0.00609	1.14270	0.04894	0.06289	0.00103	390.9	6.4	356.6	12.2
NC-4-4	0.18804	0.00843	1.78050	0.07717	0.06868	0.00138	426.4	8.6	359.7	13.0
NC-4-5	0.24346	0.01638	2.62341	0.16167	0.07815	0.00171	483.9	10.6	375.7	13.9
NC-4-6	0.43837	0.01385	6.88820	0.24441	0.11396	0.00262	695.2	16.0	377.5	14.3
NC-4-7	0.53801	0.01046	10.53324	0.25418	0.14200	0.00248	856.6	14.9	362.3	12.6
NC-4-8	0.43544	0.00989	6.39034	0.15189	0.10644	0.00145	655.7	8.9	355.6	11.7
NC-4-9	0.36035	0.00912	4.55902	0.12422	0.09176	0.00152	570.1	9.3	359.3	12.3
NC-4-10	0.50380	0.00968	8.76989	0.18548	0.12625	0.00172	761.2	10.4	355.5	11.7
NC-4-11	0.33051	0.01380	3.88680	0.15648	0.08529	0.00167	524.6	10.3	353.7	12.7
NC-4-12	0.44957	0.00903	7.07033	0.14696	0.11406	0.00138	693.3	8.4	368.3	11.9
NC-4-13	0.40033	0.01119	5.60726	0.16554	0.10159	0.00181	621.7	11.1	366.4	12.8
NC-4-14	0.25863	0.01331	2.84947	0.13767	0.07991	0.00170	494.6	10.6	374.8	13.8
NC-4-15	0.37043	0.00993	4.74575	0.12719	0.09292	0.00134	572.4	8.3	356.7	11.9
NC-4-16	0.58188	0.00907	13.56160	0.23747	0.16904	0.00196	1007.4	11.7	374.1	12.0
NC-4-17	0.19329	0.00953	1.88132	0.08396	0.07059	0.00115	440.6	7.2	366.7	12.5
NC-4-18	0.34300	0.00955	4.16274	0.11568	0.08802	0.00131	545.6	8.1	356.5	11.9
NC-4-19	0.30556	0.01339	3.47589	0.12221	0.08250	0.00162	580.7	9.1	357.8	12.8
NC-4-20	0.19887	0.01154	1.99094	0.08630	0.07261	0.00143	453.2	8.9	373.9	13.4
NC-4-21	0.49132	0.01413	8.41122	0.20106	0.12416	0.00178	756.1	10.8	361.3	12.0
NC-4-22	0.27939	0.01585	3.05494	0.12834	0.07931	0.00146	492.6	9.1	359.8	12.7
NC-4-23	0.35860	0.01000	4.75796	0.11331	0.09623	0.00143	592.5	8.8	377.6	12.6
NC-4-24	0.12650	0.01112	1.13008	0.07014	0.06479	0.00134	404.5	8.4	369.7	13.5
NC-4-25	0.09585	0.01104	0.81872	0.06633	0.06195	0.00162	387.0	10.1	368.1	14.6
NC-4-26	0.15697	0.01397	1.47519	0.09410	0.06816	0.00161	424.1	10.0	372.9	14.2
NC-4-27	0.43048	0.02197	6.53874	0.38928	0.11017	0.00539	671.2	32.9	371.7	21.3
NC-4-28	0.40739	0.01780	5.95212	0.25991	0.10597	0.00343	650.3	21.0	376.2	16.6
NC-4-29	0.32806	0.01779	3.95796	0.16598	0.08750	0.00183	541.4	11.3	364.2	13.3
NC-4-30	0.37353	0.01656	5.03184	0.17928	0.09770	0.00192	601.5	11.8	372.3	13.4
NC-4-31	0.49657	0.01450	8.50196	0.22507	0.12418	0.00221	755.1	13.5	356.5	12.4
NC-4-32	0.49750	0.02135	8.60334	0.33975	0.12543	0.00340	762.0	20.6	359.1	14.5
NC-4-33	0.52493	0.01354	9.97868	0.22734	0.13787	0.00205	832.7	12.4	365.5	12.2
NC-4-34	0.43074	0.01613	6.13917	0.19022	0.10337	0.00188	634.0	11.5	349.2	12.3
NC-4-35	0.43520	0.01513	6.40534	0.19016	0.10675	0.00196	653.6	12.0	356.7	12.6
NC-4-36	0.45796	0.01537	7.10719	0.19528	0.11256	0.00178	687.1	10.9	356.5	12.1
NC-4-37	0.43701	0.01787	6.63360	0.22709	0.11009	0.00226	672.6	13.8	366.1	13.3
NC-4-38	0.41619	0.01946	6.11300	0.23155	0.10653	0.00227	651.7	13.9	371.1	13.7

Table 1 (*continued*)

| Spots	Isotopic ratios						Ages(Ma)		207Pb-Corrected ages(Ma)	
	$^{207}Pb/^{206}Pb$	2σ	$^{207}Pb/^{235}U$	2σ	$^{206}Pb/^{238}U$	2σ	$^{206}Pb/^{238}U$	2σ	$^{206}Pb/^{238}U$	2σ
NC-4-39	0.36287	0.00889	4.69427	0.12162	0.09382	0.00147	580.7	9.1	365.4	12.4
NC-4-40	0.41354	0.00850	5.97048	0.12817	0.10471	0.00133	645.6	8.1	367.1	12.0
NC-5a-1	0.21137	0.01126	2.04397	0.10576	0.07014	0.00179	435.2	11.1	356.0	14.0
NC-5a-2	0.40198	0.02109	5.62073	0.29614	0.10141	0.00288	620.9	17.7	367.8	15.2
NC-5a-3	0.41381	0.01833	5.86468	0.26006	0.10279	0.00244	629.5	15.0	363.7	13.9
NC-5a-4	0.38276	0.01226	5.24206	0.17191	0.09933	0.00184	609.9	11.3	374.5	13.2
NC-5a-5	0.44579	0.01537	6.87462	0.24398	0.11185	0.00226	684.1	13.8	368.5	13.3
NC-5a-6	0.47545	0.01609	7.36354	0.26653	0.11233	0.00249	688.9	15.2	345.4	12.9
NC-5a-7	0.25292	0.01560	2.59873	0.15994	0.07452	0.00245	464.8	15.2	354.8	15.8
NC-5a-8	0.49530	0.01247	8.72400	0.22761	0.12775	0.00194	776.9	11.7	372.8	12.5
NC-5a-9	0.08736	0.00549	0.72386	0.04065	0.06009	0.00111	376.4	7.0	361.4	12.7
NC-5a-10	0.49424	0.01090	8.53251	0.23082	0.12521	0.00246	760.5	14.9	366.6	13.1
NC-5a-11	0.17648	0.01682	1.68915	0.14559	0.06942	0.00218	432.7	13.6	370.3	16.1
NC-5a-12	0.10122	0.00460	0.87715	0.03720	0.06285	0.00115	392.9	7.2	371.1	13.0
NC-5a-13	0.33510	0.00939	4.15544	0.12182	0.08994	0.00156	555.2	9.6	371.6	12.9
NC-5a-14	0.11934	0.00835	1.06549	0.06628	0.06475	0.00128	404.4	8.0	373.3	13.4
NC-5a-15	0.32378	0.01585	3.95765	0.20167	0.08865	0.00265	547.5	16.4	373.8	15.8
NC-5a-16	0.44452	0.01609	6.90038	0.25200	0.11259	0.00226	687.8	13.8	371.9	13.4
NC-5a-17	0.19478	0.00605	1.90282	0.05960	0.07085	0.00124	441.3	7.7	368.2	12.8
NC-5a-18	0.21939	0.01061	2.24424	0.09912	0.07419	0.00133	461.3	8.3	371.6	13.0
NC-5a-19	0.16183	0.00657	1.50904	0.05761	0.06763	0.00119	421.9	7.4	368.3	12.8
NC-5a-20	0.20902	0.01393	2.05659	0.12831	0.07136	0.00201	444.3	12.5	363.3	14.9
NC-5a-21	0.53456	0.01579	10.44573	0.32582	0.14172	0.00271	854.4	16.3	371.5	13.2
NC-5a-22	0.24216	0.01073	2.42905	0.10552	0.07275	0.00165	452.7	10.3	352.4	13.3
NC-5a-23	0.09510	0.00521	0.82807	0.04117	0.06316	0.00122	394.8	7.6	375.7	13.4
NC-5a-24	0.36591	0.01848	4.74853	0.19548	0.09412	0.00225	577.2	13.9	367.1	14.1
NC-5a-25	0.45459	0.01924	6.97753	0.25233	0.11132	0.00254	682.3	15.5	359.6	13.5
NC-5a-26	0.52644	0.02778	9.50088	0.52819	0.13089	0.00565	799.5	34.2	351.7	18.5
NC-5a-27	0.30042	0.01453	3.39083	0.13047	0.08186	0.00171	515.7	10.6	360.1	13.2
NC-5a-28	0.58367	0.01803	13.26571	0.44565	0.16484	0.00437	996.6	26.1	370.8	14.8
NC-5a-29	0.35035	0.01619	4.32065	0.14971	0.08944	0.00141	558.1	8.7	359.6	12.2
NC-5a-30	0.32210	0.01672	3.77344	0.14982	0.08497	0.00165	529.7	10.2	359.8	12.9
NC-5a-31	0.22828	0.01295	2.31251	0.09912	0.07347	0.00147	459.1	9.2	363.3	13.1
NC-5a-32	0.32201	0.02618	3.74844	0.24034	0.08443	0.00288	523.3	17.8	357.6	16.3
NC-5a-33	0.10695	0.01339	0.94479	0.08260	0.06407	0.00164	399.7	10.2	375.4	14.8
NC-5a-34	0.58866	0.02732	13.47704	0.56097	0.16605	0.00461	977.3	27.5	367.3	15.0
NC-5b-1	0.50466	0.01092	9.05750	0.22918	0.13017	0.00224	781.9	13.6	360.9	12.5
NC-5b-2	0.43327	0.01348	6.53300	0.22772	0.10936	0.00246	664.3	15.0	363.6	13.6
NC-5b-3	0.39359	0.01728	5.26493	0.24933	0.09702	0.00279	593.7	17.2	352.7	14.7
NC-5b-4	0.45523	0.01263	7.38514	0.20835	0.11766	0.00179	714.6	10.9	371.0	12.5
NC-5b-5	0.20738	0.01193	1.99570	0.10815	0.06980	0.00158	434.2	9.8	354.6	13.3
NC-5b-6	0.15661	0.01118	1.48804	0.09951	0.06891	0.00187	429.6	11.7	376.5	15.2
NC-5b-7	0.32732	0.01239	3.97731	0.15094	0.08813	0.00174	545.4	10.8	365.4	13.1
NC-5b-8	0.17303	0.00924	1.60870	0.08209	0.06743	0.00153	422.2	9.5	360.4	13.5
NC-5b-9	0.33746	0.01301	4.02906	0.16127	0.08660	0.00196	538.3	12.1	352.6	13.3
NC-5b-10	0.68418	0.01070	25.30480	0.82407	0.26825	0.00796	1542.1	45.4	370.0	15.6
NC-5b-11	0.18692	0.01312	1.79322	0.11443	0.06958	0.00164	430.6	10.2	364.2	13.9
NC-5b-12	0.42015	0.01416	6.16969	0.23499	0.10650	0.00271	649.5	16.6	364.9	14.3
NC-5b-13	0.36851	0.01116	4.82655	0.14799	0.09499	0.00162	583.9	10.0	363.5	12.5
NC-5b-14	0.34993	0.01569	4.29745	0.20326	0.08907	0.00254	549.7	15.7	354.0	14.6
NC-5b-15	0.51925	0.01063	9.51053	0.22202	0.13284	0.00209	804.6	12.7	353.5	12.0
NC-5b-16	0.42369	0.01113	6.13626	0.16458	0.10504	0.00159	645.1	9.8	357.2	12.0
NC-5b-17	0.19564	0.01210	1.87591	0.10926	0.06954	0.00181	434.8	11.3	359.5	14.3
NC-5b-18	0.35322	0.00989	4.46792	0.12740	0.09174	0.00147	568.3	9.1	362.0	12.3
NC-5b-19	0.56772	0.01362	12.85525	0.38827	0.16423	0.00369	985.6	22.0	374.6	14.0
NC-5b-20	0.64232	0.02104	19.00097	0.70455	0.21455	0.00649	1248.9	37.9	365.6	15.6
NC-5b-21	0.51766	0.01953	9.51286	0.29981	0.13328	0.00261	804.8	15.8	356.2	12.8
NC-5b-22	0.37512	0.01717	5.19231	0.19187	0.10039	0.00217	615.7	13.3	378.6	14.0
NC-5b-23	0.22218	0.01623	2.22713	0.11792	0.07270	0.00165	452.0	10.3	360.8	13.6
NC-5b-24	0.58163	0.01799	13.07673	0.34035	0.16306	0.00267	973.5	15.9	354.9	12.1
NC-5b-25	0.43332	0.01911	6.64743	0.23609	0.11126	0.00230	680.3	14.1	369.7	13.5
NC-5b-26	0.46012	0.01813	7.13303	0.23682	0.11244	0.00235	687.5	14.4	350.8	12.8
NC-5b-27	0.50927	0.01831	9.59203	0.30244	0.13660	0.00287	826.7	17.3	373.4	13.7
NC-5b-28	0.46992	0.01898	7.66523	0.25848	0.11830	0.00248	722.4	15.1	359.9	13.2
NC-5b-29	0.28062	0.02497	3.13136	0.21360	0.08093	0.00288	503.1	17.8	364.8	17.0
NC-5b-30	0.35382	0.01797	4.75351	0.19448	0.09744	0.00225	610.8	13.8	383.4	14.5
NC-5b-31	0.46859	0.01506	8.22664	0.25487	0.12733	0.00286	784.5	17.3	387.8	14.5
NC-5b-32	0.42620	0.01598	6.23045	0.21397	0.10603	0.00250	657.5	15.3	358.5	13.7
NC-5b-33	0.26654	0.01311	2.93731	0.11444	0.07993	0.00169	500.0	10.5	368.9	13.5
NC-5b-34	0.25145	0.01259	2.63754	0.10102	0.07608	0.00144	475.1	9.0	360.3	12.8
NC-5b-35	0.58866	0.02732	13.47471	0.56097	0.16602	0.00461	977.3	27.5	352.4	14.4
NC-5b-36	0.35163	0.01944	4.74871	0.20267	0.09795	0.00212	597.2	13.1	387.0	14.3
NC-5b-37	0.50514	0.01898	8.80528	0.28700	0.12643	0.00265	758.3	16.1	350.3	12.8
NC-5b-38	0.48892	0.01706	8.19146	0.25104	0.12151	0.00243	727.9	14.8	351.9	12.7
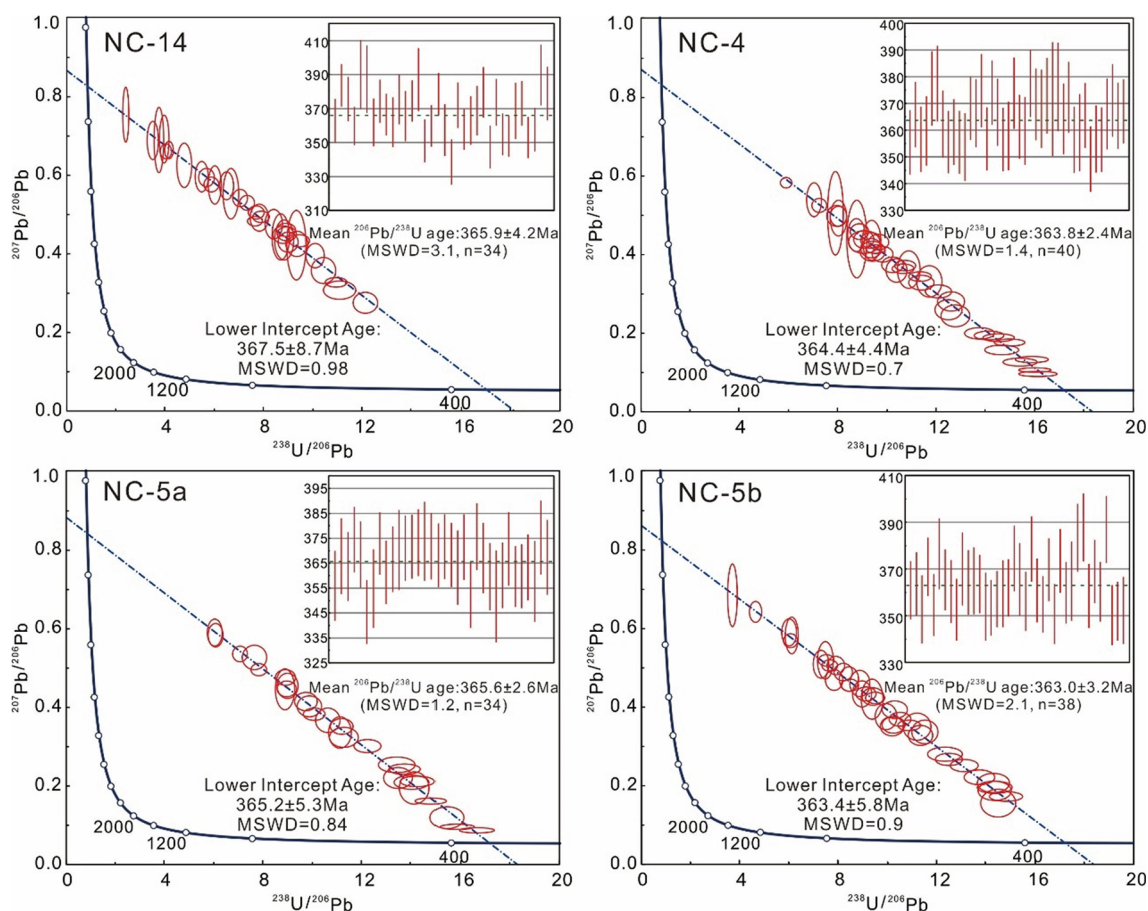
Fig. 6. Tera-Wasserburg and weighted average diagrams for the cassiterite in different mineralization styles from the Neves Corvo deposit. NC-14: fissural cassiterite ore (FT); NC-4: massive cassiterite ore (MT); NC-5a, 5b: rubané cassiterite ore (RT).

Neves Corvo lacks any sulfate and Fe oxides in its mineral assemblages, and it is hosted in organic-rich shales. This, together with the presence of arsenopyrite and pyrrhotite in the massive sulfide ores (Gaspar, 2002; Carvalho et al., 2018), suggests that the Neves Corvo ore fluids were at low oxidation potential there was little or no subsequent oxidation, and that the $\delta^{34}S$ values of the sulfide minerals closely reflects the $\delta^{34}S$ of the hydrothermal solutions (Ohmoto, 1972). In contrast, microbiologically related sulfide precipitation is associated with a $\delta^{34}S$ fractionation, ranging from 15 to 71‰, (Goldhaber et al., 1975). Considering that sulfate had a $\delta^{34}S$ of about 23‰ (Kampschulte and Strauss, 2004) in Lower Carboniferous seawater, this would result in sulfides with $\delta^{34}S$ between −48‰ and +8‰. Hence microbial sulfate reduction likely accounts for the more negative $\delta^{34}S$ values (as low as −32.3‰) in the MS and MC massive sulfide ores (Fig. 7). The fissural ores show more positive $\delta^{34}S$ values than the massive sulfide ores, which may indicate entrainment of sulfur from other sources. Sulfur derived from thermochemical sulfate reduction has a 0–25‰ lighter $\delta^{34}S$ value than the seawater sulfate from which it was derived (Velasco et al., 1998) and would result in sulfides with $\delta^{34}S$ values between −2‰ and +23‰. This range encompasses that observed in sulfides from the fissural ores ($\delta^{34}S$ = −0.5 to +12.5‰) and rubané ores ($\delta^{34}S$ = +1.7 to +4.8‰) (Fig. 7). Thermochemical seawater sulfate reduction has also been suggested as a source of sulfide in other contemporaneous VMS deposits in the IPB (Velasco et al., 1998). In contrast, the limited ranges in $\delta^{34}S$ values (clustered near 0‰) in the Sn-rich ores, likely reflects a magmatic source of sulfur, either by leaching of magmatic rocks or directly from magmatic fluids.

5.3. Genetic model for the Neves Corvo deposit

There are two main models for VMS formation: one is the Kuroko-type, with sulfides deposited from exhaling, buoyant, seawater-dominated fluids that mixed with seawater to form sulfate-sulfide mounds (Ohmoto, 1996), and the other is the brine-pool model, with sulfides precipitating in hot, dense brine filled basins or pools (Solomon and Zaw, 1997). The geological and textural features of the orebodies, and the presence of high-salinity metallogenic fluids are interpreted by a number of authors as favoring a brine-pool model for the IPB deposits in general (Inverno et al., 2008; Sánchez-España et al., 2003; Tornos et al., 2008). The lack of evidence for chimney formation and collapse, and the absence of rubble mounds suggest that processes observed in Kuroku-type ores were not significant in Neves Corvo ore formation. The absence of barite in the Neves Corvo massive orebodies also contrasts with the sulfate-rich Kuroko ores found in the Hokuroku basin. The presence of local bacterial sulfate reduction, evidenced by the $\delta^{34}S$ data, also give a supports the conclusion that the style of mineralization at the Neves Corvo deposit does not correspond to a mound-like depositional setting. Instead, Solomon et al. (2004) proposed that the Neves Corvo sulfides were deposited in a brine pool. While the replacement mechanisms of subsurface deposition seem more plausible to explain the textural and geometric features observed in some parts of the deposit (e.g. Relvas et al., 2006a), we suggest the brine-pool model applied to the mineralization style of the Neves Corvo massive orebodies.

Although the host sequence to the Neves Corvo deposit is similar to other IPB deposits in terms of geochemistry, lithology and volcanology,

Table 2
LA-MC-ICPMS δ^{34}S isotopic data for sulfides from the Neves Corvo deposit.

Spots	δ^{34}S‰	Mineral	Ore type	Spots	δ^{34}S‰	Minerals	Ore type
NC-7a-1	2.4	Py	FC	NC-2-21	17.4	Py	MS
NC-7a-2	2.2	Py	FC	NC-2-22	−6.6	Ccp	MS
NC-7a-3	2.1	Py	FC	NC-2-23	−4.2	Ccp	MS
NC-7a-4	2.4	Py	FC	NC-2-24	−5.0	Ccp	MS
NC-7a-5	2.3	Py	FC	NC-2-25	−3.5	Ccp	MS
NC-7a-6	2.6	Ccp	FC	NC-2-26	−4.1	Ccp	MS
NC-7a-7	2.2	Ccp	FC	NC-2-27	−2.3	Ccp	MS
NC-7a-8	2.6	Ccp	FC	NC-2-28	−1.5	Ccp	MS
NC-7a-9	2.7	Ccp	FC	NC-2-29	−0.5	Ccp	MS
NC-7a-10	2.2	Ccp	FC	NC-2-30	3.4	Py	MS
NC-7a-11	2.1	Ccp	FC	NC-2-31	3.7	Py	MS
NC-7a-12	2.2	Ccp	FC	NC-2-32	3.5	Py	MS
NC-7a-13	2.3	Ccp	FC	NC-2-33	3.5	Py	MS
NC-7a-14	2.1	Py	FC	NC-2-34	3.3	Py	MS
NC-7a-15	1.8	Py	FC	NC-2-35	3.0	Py	MS
NC-7a-16	2.1	Py	FC	NC-6-1	−0.4	Sp	MS
NC-7a-17	2.7	Py	FC	NC-6-2	−3.7	Sp	MS
NC-7a-18	1.9	Py	FC	NC-6-3	−2.5	Ccp	MS
NC-7a-19	2.8	Py	FC	NC-6-4	6.1	Py	MS
NC-7a-20	2.1	Py	FC	NC-6-5	10.4	Py	MS
NC-7a-21	2.5	Py	FC	NC-6-6	−3.3	Py	MS
NC-7a-22	1.9	Ccp	FC	NC-6-7	−2.9	Py	MS
NC-7a-23	2.3	Ccp	FC	NC-6-8	−1.0	Py	MS
NC-7a-24	11.0	Py	FC	NC-6-9	2.8	Py	MS
NC-7a-25	6.2	Py	FC	NC-6-10	2.8	Py	MS
NC-7a-26	2.0	Ccp	FC	NC-6-11	8.7	Py	MS
NC-7a-27	2.3	Ccp	FC	NC-6-12	7.6	Py	MS
NC-7a-28	2.8	Py	FC	NC-6-13	9.3	Py	MS
NC-7a-29	2.9	Py	FC	NC-6-14	8.4	Py	MS
NC-7a-30	1.6	Py	FC	NC-6-15	−1.6	Ccp	MS
NC-7a-31	2.6	Ccp	FC	NC-6-16	−2.4	Ccp	MS
NC-7b-1	1.1	Ccp	FC	NC-6-17	−1.2	Ccp	MS
NC-7b-2	1.1	Ccp	FC	NC-6-18	−3.7	Ccp	MS
NC-7b-3	1.2	Ccp	FC	NC-6-19	−14.9	Py	MS
NC-7b-4	0.9	Py	FC	NC-6-20	−26.2	Py	MS
NC-7b-5	4.1	Py	FC	NC-6-21	−27.7	Py	MS
NC-7b-6	1.6	Py	FC	NC-6-22	−27.1	Py	MS
NC-7b-7	1.1	Py	FC	NC-6-23	−26.8	Py	MS
NC-7b-8	1.5	Py	FC	NC-6-24	0.5	Sp	MS
NC-7b-9	1.0	Py	FC	NC-6-25	1.4	Ccp	MS
NC-7b-10	1.0	Ccp	FC	NC-6-26	0.1	Ccp	MS
NC-7b-11	1.1	Ccp	FC	NC-6-27	1.5	Ccp	MS
NC-7b-12	0.7	Ccp	FC	NC-6-28	−18.1	Py	MS
NC-7b-13	−0.5	Py	FC	NC-6-29	−27.5	Py	MS
NC-7b-14	1.5	Py	FC	NC-6-30	−29.0	Py	MS
NC-7b-15	2.2	Py	FC	NC-4-1	1.5	Py	MT
NC-7b-16	1.3	Py	FC	NC-4-2	1.0	Py	MT
NC-7b-17	1.5	Py	FC	NC-4-3	0.8	Py	MT
NC-7b-18	1.9	Py	FC	NC-4-4	0.4	Py	MT
NC-7b-19	0.7	Ccp	FC	NC-4-5	0.5	Py	MT
NC-7b-20	1.0	Ccp	FC	NC-4-6	−0.4	Ccp	MT
NC-9-1	2.9	Ccp	FC	NC-4-7	−0.6	Ccp	MT
NC-9-2	2.5	Ccp	FC	NC-4-8	−0.9	Ccp	MT
NC-9-3	2.8	Ccp	FC	NC-4-9	−0.6	Ccp	MT
NC-9-4	2.8	Ccp	FC	NC-4-10	−0.4	Ccp	MT
NC-9-5	2.7	Ccp	FC	NC-4-11	1.0	Py	MT
NC-9-6	2.6	Ccp	FC	NC-4-12	0.7	Sp	MT
NC-9-7	12.5	Py	FC	NC-4-13	−0.1	Sp	MT
NC-9-8	11.3	Py	FC	NC-4-14	0.0	Sp	MT
NC-9-9	12.2	Py	FC	NC-4-15	0.1	Sp	MT
NC-9-10	8.4	Py	FC	NC-4-16	0.2	Py	MT
NC-9-11	8.6	Py	FC	NC-4-17	0.0	Py	MT
NC-9-12	8.8	Py	FC	NC-4-18	0.0	Py	MT
NC-9-13	9.3	Py	FC	NC-4-19	0.0	Py	MT
NC-9-14	11.6	Py	FC	NC-4-20	−0.1	Py	MT
NC-9-15	3.6	Ccp	FC	NC-12-1	−0.2	Ccp	MZ
NC-9-16	3.5	Ccp	FC	NC-12-2	−0.6	Ccp	MZ
NC-14-1	2.9	Py	FT	NC-12-3	0.2	Ccp	MZ
NC-14-2	2.6	Py	FT	NC-12-4	0.1	Ccp	MZ
NC-14-3	2.4	Py	FT	NC-12-5	1.8	Ccp	MZ
NC-14-4	2.2	Py	FT	NC-12-6	1.9	Ccp	MZ
NC-14-5	2.2	Py	FT	NC-12-7	2.7	Py	MZ
NC-14-6	2.1	Py	FT	NC-12-8	2.7	Py	MZ
NC-14-7	2.5	Py	FT	NC-12-9	2.9	Py	MZ

Table 2 (continued)

Spots	δ³⁴S‰	Mineral	Ore type	Spots	δ³⁴S‰	Minerals	Ore type
NC-14-8	3.1	Py	FT	NC-12-10	4.1	Py	MZ
NC-14-9	3.1	Py	FT	NC-12-11	3.2	Py	MZ
NC-14-10	2.7	Py	FT	NC-12-12	1.3	Sp	MZ
NC-14-11	2.4	Py	FT	NC-12-13	1.8	Sp	MZ
NC-14-12	1.8	Py	FT	NC-12-14	2.2	Sp	MZ
NC-14-13	1.7	Py	FT	NC-12-15	1.4	Sp	MZ
NC-14-14	1.8	Py	FT	NC-12-16	2.5	Sp	MZ
NC-14-15	1.7	Py	FT	NC-12-17	0.7	Ccp	MZ
NC-14-16	1.3	Py	FT	NC-12-18	1.1	Ccp	MZ
NC-14-17	1.4	Py	FT	NC-12-19	0.7	Ccp	MZ
NC-14-18	0.7	Py	FT	NC-12-20	4.1	Py	MZ
NC-14-19	2.2	Py	FT	NC-12-21	2.7	Py	MZ
NC-14-20	2.2	Py	FT	NC-12-22	2.6	Py	MZ
NC-14-21	2.0	Py	FT	NC-12-23	2.2	Py	MZ
NC-14-22	1.8	Py	FT	NC-12-24	1.4	Sp	MZ
NC-14-23	1.8	Py	FT	NC-12-25	1.3	Sp	MZ
NC-14-24	1.6	Py	FT	NC-12-26	1.0	Sp	MZ
NC-14-25	2.8	Py	FT	NC-12-27	2.8	Py	MZ
NC-1-1	4.9	Py	MC	NC-12-28	2.6	Py	MZ
NC-1-2	6.5	Py	MC	NC-12-29	2.5	Py	MZ
NC-1-3	4.5	Py	MC	NC-12-30	1.0	Sp	MZ
NC-1-4	4.1	Py	MC	NC-12-31	0.1	Sp	MZ
NC-1-5	7.1	Py	MC	NC-12-32	0.1	Sp	MZ
NC-1-6	4.5	Py	MC	NC-12-33	1.9	Py	MZ
NC-1-7	3.8	Py	MC	NC-12-34	0.4	Py	MZ
NC-1-8	2.8	Py	MC	NC-12-35	0.8	Ccp	MZ
NC-1-9	2.4	Py	MC	NC-12-36	1.0	Ccp	MZ
NC-1-10	2.6	Py	MC	NC-12-37	1.6	Ccp	MZ
NC-1-11	0.0	Ccp	MC	NC-12-38	1.8	Ccp	MZ
NC-1-12	−0.3	Ccp	MC	NC-12-39	2.8	Ccp	MZ
NC-1-13	0.2	Ccp	MC	NC-10-1	2.4	Py	RC
NC-1-14	3.0	Py	MC	NC-10-2	1.8	Py	RC
NC-1-15	−0.5	Ccp	MC	NC-10-3	1.9	Py	RC
NC-1-16	0.1	Ccp	MC	NC-10-4	1.8	Ccp	RC
NC-1-17	1.6	Py	MC	NC-10-5	2.5	Ccp	RC
NC-1-18	4.7	Py	MC	NC-10-6	2.3	Ccp	RC
NC-1-19	0.9	Py	MC	NC-10-7	3.3	Ccp	RC
NC-1-20	1.0	Py	MC	NC-10-8	3.1	Py	RC
NC-1-21	−0.5	Ccp	MC	NC-10-9	3.2	Py	RC
NC-1-22	−0.3	Ccp	MC	NC-10-10	2.6	Py	RC
NC-11-1	−6.8	Py	MC	NC-10-11	2.4	Ccp	RC
NC-11-2	−6.8	Py	MC	NC-10-12	2.4	Ccp	RC
NC-11-3	−6.4	Sp	MC	NC-10-13	2.6	Py	RC
NC-11-4	−7.0	Sp	MC	NC-10-14	2.3	Py	RC
NC-11-5	−6.2	Py	MC	NC-10-15	2.1	Py	RC
NC-11-6	−6.1	Py	MC	NC-10-16	2.1	Py	RC
NC-11-7	−6.5	Py	MC	NC-10-17	3.6	Ccp	RC
NC-11-8	−6.9	Py	MC	NC-10-18	3.4	Ccp	RC
NC-11-9	−8.4	Ccp	MC	NC-10-19	3.3	Ccp	RC
NC-11-10	−8.3	Ccp	MC	NC-10-20	2.5	Py	RC
NC-11-11	−6.7	Sp	MC	NC-10-21	2.9	Py	RC
NC-11-12	−6.9	Sp	MC	NC-10-22	2.1	Py	RC
NC-11-13	−6.1	Sp	MC	NC-10-23	1.7	Py	RC
NC-11-14	−6.5	Py	MC	NC-10-24	4.5	Sp	RC
NC-11-15	−6.9	Py	MC	NC-10-25	4.5	Sp	RC
NC-11-16	−7.2	Py	MC	NC-10-26	3.9	Sp	RC
NC-11-17	−7.4	Py	MC	NC-5a-1	4.4	Sp	RT
NC-11-18	−7.2	Ccp	MC	NC-5a-2	3.5	Sp	RT
NC-11-19	−7.4	Py	MC	NC-5a-3	3.7	Sp	RT
NC-11-20	−7.3	Py	MC	NC-5a-4	4.8	Sp	RT
NC-11-21	−6.4	Py	MC	NC-5a-5	4.2	Ccp	RT
NC-11-22	−7.4	Py	MC	NC-5a-6	3.5	Ccp	RT
NC-11-23	−7.5	Py	MC	NC-5a-7	3.2	Py	RT
NC-11-24	−6.8	Sp	MC	NC-5a-8	2.4	Py	RT
NC-11-25	−5.9	Sp	MC	NC-5a-9	3.6	Ccp	RT
NC-11-26	−7.1	Ccp	MC	NC-5b-1	2.9	Py	RT
NC-11-27	−6.0	Ccp	MC	NC-5b-2	3.0	Py	RT
NC-11-28	−6.4	Ccp	MC	NC-5b-3	2.9	Py	RT
NC-11-29	−6.3	Ccp	MC	NC-5b-4	3.2	Py	RT
NC-11-30	−6.0	Ccp	MC	NC-5b-5	3.2	Py	RT
NC-11-31	−5.9	Sp	MC	NC-5b-6	2.5	Py	RT
NC-11-32	−6.4	Sp	MC	NC-5b-7	2.8	Py	RT
NC-11-33	−6.4	Py	MC	NC-5b-8	2.2	Py	RT
NC-11-34	−6.9	Py	MC	NC-5b-9	2.4	Py	RT
NC-11-35	−6.6	Py	MC	NC-5b-10	3.3	Ccp	RT

Table 2 (*continued*)

Spots	δ³⁴S‰	Mineral	Ore type	Spots	δ³⁴S‰	Minerals	Ore type
NC-11-36	−6.5	Py	MC	NC-5b-11	3.2	Sp	RT
NC-11-37	−5.9	Py	MC	NC-5b-12	3.4	Sp	RT
NC-11-38	−5.4	Ccp	MC	NC-5b-13	3.3	Ccp	RT
NC-11-39	−6.6	Ccp	MC	NC-5b-14	3.3	Ccp	RT
NC-11-40	−6.4	Sp	MC	NC-5b-15	3.3	Sp	RT
NC-11-41	−6.3	Sp	MC	NC-5a-10	2.8	Ccp	RT
NC-11-42	−1.8	Py	MC	NC-5a-11	1.7	Ccp	RT
NC-11-43	−2.0	Py	MC	NC-5a-12	2.9	Ccp	RT
NC-11-44	−9.6	Py	MC	NC-5a-13	1.9	Ccp	RT
NC-11-45	−7.0	Sp	MC	NC-5a-14	1.9	Ccp	RT
NC-11-46	−6.3	Sp	MC	NC-13-1	5.1	Py	ME
NC-11-47	−7.6	Ccp	MC	NC-13-2	9.9	Py	ME
NC-11-48	−5.0	Py	MC	NC-13-3	5.5	Py	ME
NC-11-49	−12.8	Py	MC	NC-13-4	7.8	Py	ME
NC-11-50	−6.0	Py	MC	NC-13-5	6.2	Py	ME
NC-2-1	−4.2	Ccp	MS	NC-13-6	6.3	Py	ME
NC-2-2	−5.5	Ccp	MS	NC-13-7	6.1	Py	ME
NC-2-3	−5.6	Ccp	MS	NC-13-8	7.1	Py	ME
NC-2-4	−5.9	Ccp	MS	NC-13-9	7.4	Py	ME
NC-2-5	−6.1	Ccp	MS	NC-13-10	9.4	Py	ME
NC-2-6	−24.5	Py	MS	NC-13-11	5.4	Py	ME
NC-2-7	−32.3	Py	MS	NC-13-12	7.3	Py	ME
NC-2-8	−26.7	Py	MS	NC-13-13	9.4	Py	ME
NC-2-9	−11.5	Ccp	MS	NC-13-14	7.7	Py	ME
NC-2-10	−30.3	Py	MS	NC-13-15	3.9	Ccp	ME
NC-2-11	−27.5	Py	MS	NC-13-16	3.4	Ccp	ME
NC-2-12	−32.3	Py	MS	NC-13-17	2.5	Ccp	ME
NC-2-13	−31.2	Py	MS	NC-13-18	3.3	Ccp	ME
NC-2-14	17.3	Py	MS	NC-13-19	4.6	Py	ME
NC-2-15	16.6	Py	MS	NC-13-20	5.1	Py	ME
NC-2-16	15.3	Py	MS	NC-13-21	4.7	Py	ME
NC-2-17	15.8	Py	MS	NC-13-22	5.6	Py	ME
NC-2-18	14.0	Py	MS	NC-13-23	6.3	Py	ME
NC-2-19	−3.8	Ccp	MS	NC-13-24	6.4	Py	ME
NC-2-20	−3.8	Ccp	MS	NC-13-25	4.3	Py	ME

Abbreviations: Py-pyrite, Ccp-chalcopyrite, Sp-sphalerite, FC- copper-rich stringer ore, FT-fissural stanniferous ore, MC- copper-rich massive sulfide ore, MS- high copper and tin contents massive sulfide ore, MT- massive cassiterite ore, MZ- zinc-rich massive sulfide ore, RC- rubané cupriferous ore, RT- rubané stanniferous ore, ME-barren massive sulfides ore.

the geochemical characteristics of the Sn-rich mineralization are distinct. The synchronicity between the U-Pb dates of the cassiterite and the upwelling of the magmatic hydrothermal fluids, and the limited ranges in δ³⁴S values clustered near 0‰ in the Sn-rich ores, support a magmatic fluid source of the Sn enrichment that was near synchronous with deposition of the massive sulfide ores. While granitic plutons are not exposed in the immediate area of Neves Corvo, melt inclusions in quartz phenocrysts from the felsic volcanic rocks have similar compositions to those in tin granites, which raise the possibility of the presence a tin-rich granite at depth (Tornos, 2004). In this regard, Sn may have been derived from a granitic pluton that is probably present at

depth. In this model, focused discharge of large volumes of concentrated tin-bearing fluids vented into a deep basin and lost all their contained H₂S by precipitation of small amounts of sulfides due to quenching, leading to the formation of tin-rich ores.

Overall, this study provides tightly constrained geochronologic and sulfur isotope data that provide the strongest evidence to date that incorporation of magmatic hydrothermal fluids into a VMS hydrothermal system led directly to the deposition of large-scale and high-grade Sn ores, and Cu-Sn metal association in the Neves Corvo deposit; consistent with the metallogenic model proposed by Relvas et al. (2001, 2006b).
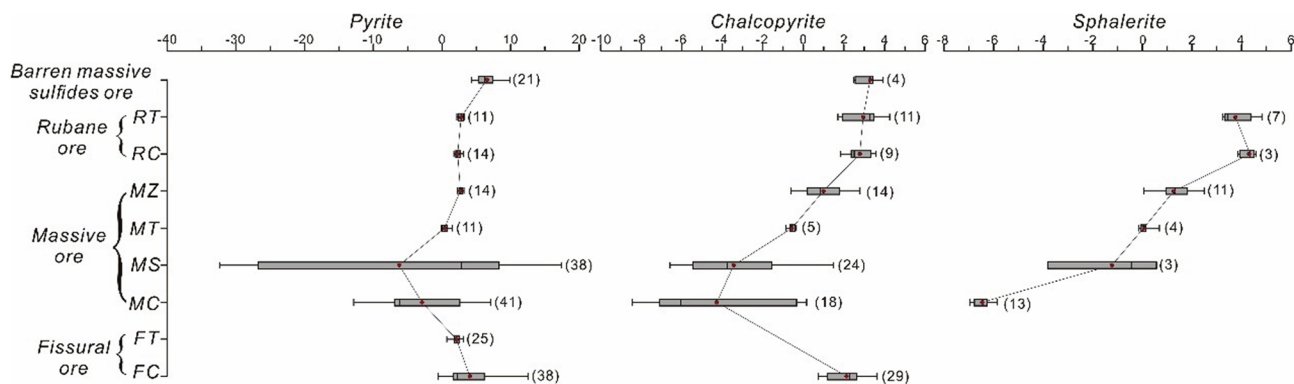

Fig. 7. Box-Whisker plot showing the variations in δ³⁴S values of sulfides from the different mineralization styles of the Neves Corvo deposit. The width of the box is proportional to the half width (75th percentile–25th percentile). The central line in the box represents the median. The whiskers represent the extent of the dataset. The red dot in the box represents the mean value. The numbers between parentheses represent the number of data points analyzed.

6. Conclusion

LA-ICP-MS U-Pb dating of four hydrothermal cassiterite samples from three different ore types from the Neves Corvo deposit defines a tin mineralization age of 363–366 Ma, which is synchronous with the felsic volcanic activity in this region. The sulfur isotope data indicate the massive sulfide ores have the most negative $\delta^{34}S$ values and indicate a component derived from the microbiological reduction of seawater sulfate, while the stockwork vein sulfides contain a significant contribution from the thermal reduction of seawater sulfate. The $\delta^{34}S$ values of the tin-rich ores are most compatible with a magmatic sulfur source. Overall, the data presented here are most consistent with a model for tin mineralization that involves magmatic fluids exsolved from a granitic that was near synchronous with deposition of the typical VMS deposits of the IPB.

Acknowledgements

Appendix A. Supplementary data

Supplementary data to this article can be found online at https://doi.org/10.1016/j.oregeorev.2018.12.023.

References

Cabri, L.J., Gaspar, O.C., Lastra, R., Mcmahon, G., 1998. Distribution of gold in tin-rich samples from the Corvo orebody. Portugal. Can. Mineral. 36, 1347–1360.

Carvalho, J.R.S., Relvas, J.M.R.S., Pinto, A.M.M., Frenzel, M., Krause, J., Gutzmer, J., Pacheco, N., Fonseca, R., Santos, S., Caetano, P., Reis, T., Gonçalves, M., 2018. Indium and selenium distribution in the Neves-Corvo deposit, Iberian Pyrite Belt. Portugal. Mineral. Mag. 82 (S1), S5–S41.

Gaspar, O.C., 2002. Mineralogy and sulfide mineral chemistry of the Neves-Corvo ores, Portugal: insight into their genesis. Can. Mineral. 40, 611–636.

Goldhaber, M.B., Kaplan, I.R., 1975. Controls and consequences of sulfate reduction rates in recent marine sediments. Soil Sci. 119, 42–55.

Gulson, B.L., Jones, M.T., 1992. Cassiterite: potential for direct dating of mineral deposits and a precise age for the Bushveld Complex granites. Geology 20, 355–3582.

Heinrich, C.A., 1990. The chemistry of hydrothermal tin (-tungsten) ore deposition. Econ. Geol. 85, 457–481.

Huston, D.L., Relvas, J.M.R.S., Gemmell, J.B., Drieberg, S., 2011. The role of granites in volcanic-hosted massive sulphide ore-forming systems: an assessment of magmatic-hydrothermal contributions. Mineral. Deposit. 46, 473–507.

Inverno, C., Díez-Montes, A., Rosa, C., García-Crespo, J., Matos, J., García-Lobón, J.L., Carvalho, J., Bellido, F., Castello-Branco, J.M., Ayala, C., 2015. In: Introduction and Geological Setting of the Iberian Pyrite Belt. Springer International Publishing, pp. 191–208.

Inverno, C.M.C., Solomon, M., Barton, M.D., Foden, J., 2008. The Cu stockwork and massive sulfide ore of the Feitais volcanic-hosted massive sulfide deposit, Aljustrel, Iberian Pyrite Belt, Portugal: a mineralogical, fluid inclusion, and isotopic investigation. Econ. Geol. 103, 241–267.

Kampschulte, A., Strauss, H., 2004. The sulfur isotopic evolution of Phanerozoic seawater based on the analysis of structurally substituted sulfate in carbonates. Chem. Geol. 204, 255–286.

Lehmann, B., 1990. Metallogeny of Tin. Springer, Berlin Heidelberg.

Ludwig, K.R., 2012. Isoplot: A geochronological toolkit for Microsoft Excel. Special Publication no. 5. Berkeley Geochronology Center.

Marcoux, E., Moëlo, Y., Leistel, J.M., 1996. Bismuth and cobalt minerals as indicators of stringer zones to massive sulfide deposits, Iberian Pyrite Belt. Mineral. Deposit. 31, 1–26.

Mathur, R., Ruiz, J., Tornos, F., 1999. Age and sources of the ore at Tharsis and Rio Tinto, Iberian Pyrite Belt, from Re-Os isotopes. Mineral. Deposit. 34, 790–793.

Moura, A., 2005. Fluids from the Neves Corvo massive sulphide ores, Iberian Pyrite Belt. Portugal. Chem. Geol. 223, 153–169.

Moura, A., 2008. Metamorphosed and metamorphogenic ores of the Neves Corvo volcanogenic massive sulfide deposit, Iberian Pyrite Belt. Portugal. Int. Geol. Rev. 50, 89–969.

Munhá, J., 1990. Metamorphic evolution of the South Portuguese/Pulo Do Lobo Zone. In: Dallmeyer, R.D., Garcia, E.M. (Eds.), Pre-Mesozoic Geology of Iberia. Springer, Berlin Heidelberg, pp. 363–368.

Munhá, J., Relvas, J.M.R.S., Barriga, F.J.A.S., Conceição, P., Jorge, R.C.G.S., Mathur, R., Ruiz, J., Tassinari, C.C.G., 2005. Osmium isotope systematics in the Iberian Pyrite Belt. In: Mao, J., Bierlein, F.P. (Eds.), Mineral Deposit Research: Meeting the Global Challenge. Springer, Berlin Heidelberg, pp. 663–666.

Ohmoto, H., 1972. Systematics of sulfur and carbon isotopes in hydrothermal ore deposits. Econ. Geol. 67, 551–578.

Ohmoto, H., 1996. Formation of volcanogenic massive sulfide deposits: the Kuroko perspective. Ore Geol. Rev. 10, 135–177.

Oliveira, J.T.S., Pereira, Z.L., Carvalho, P., Pacheco, N., Korn, D., 2004. Stratigraphy of the tectonically imbricated lithological succession of the Neves Corvo mine area, Iberian Pyrite Belt. Portugal. Mineral. Deposit. 39, 422–436.

Oliveira, J.T., Rosa, C.J.P., Pereira, Z., Rosa, D.R.N., Matos, J.X., Inverno, C.M.C., Andersen, T., 2013. Geology of the Rosário-Neves Corvo antiform, Iberian Pyrite Belt, Portugal: new insights from physical volcanology, palynostratigraphy and isotope geochronology studies. Mineral. Deposit. 48, 749–766.

Relvas, J.M.R.S., Tassinari, C.C., Munhá, J., Barriga, F.J., 2001. Multiple sources for ore-forming fluids in the Neves Corvo VHMS Deposit of the Iberian Pyrite Belt (Portugal): strontium, neodymium and lead isotope evidence. Mineral. Deposit. 36, 416–427.

Relvas, J.M.R.S., Barriga, F.J.A.S., Ferreira, A., Noiva, P.C., Pacheco, N., Barriga, G., 2006a. Hydrothermal alteration and mineralization in the Neves-Corvo volcanic-hosted massive sulfide deposit, Portugal. I. Geol., Mineral. Geochem. Econ. Geol. 101, 753–790.

Relvas, J.M.R.S., Barriga, F.J.A.S., Longstaffe, F.J., 2006b. Hydrothermal alteration and mineralization in the Neves-Corvo volcanic-hosted massive sulfide deposit, Portugal. II. Oxygen, hydrogen, and carbon isotopes. Econ. Geol. 101, 791–804.

Rosa, C.J.P., Mcphie, J., Relvas, J.M.R.S., Pereira, Z., Oliveira, T., Pacheco, N., 2008. Facies analyses and volcanic setting of the giant Neves Corvo massive sulfide deposit, Iberian Pyrite Belt, Portugal. Mineral. Deposit. 43, 449–466.

Sánchez-España, J., Velasco, F., Boyce, A.J., Fallick, A.E., 2003. Source and evolution of ore-forming hydrothermal fluids in the northern Iberian Pyrite Belt massive sulphide deposits (SW Spain): evidence from fluid inclusions and stable isotopes. Mineral. Deposit. 38, 519–537.

Solomon, M., Tornos, F., Large, R.R., Badham, J.N.P., Both, R.A., Zaw, K., 2004. Zn-Pb-Cu volcanic-hosted massive sulphide deposits: criteria for distinguishing brine pool-type from black smoker-type sulphide deposition. Ore Geol. Rev. 25, 259–283.

Solomon, M., Zaw, K., 1997. Formation on the sea floor of the Hellyer volcanogenic massive sulfide deposit. Econ. Geol. 92, 686–695.

Stacey, J.S., Kramers, J.D., 1975. Approximation of terrestrial lead isotope evolution by a two-stage model. Earth Planet. Sci. Lett. 26, 207–221.

Taylor, J.R., Wall, V.J., 1992. The behavior of tin in granitoid magmas. Econ. Geol. 87, 403–420.

Tera, F., Wasserburg, G.J., 1972. U-Th-Pb systematics in three Apollo 14 basalts and the problem of initial Pb in lunar rocks. Earth Planet. Sci. Lett. 14, 281–304.

Tornos, F., 2004. Melt inclusions in quartz from subvolcanic sills of the Iberian Pyrite Belt: implications for magma evolution and hydrothermal alteration. Boletin de la Sociedad Espanola de Mineralogia 26, 93–105.

Tornos, F., Casquet, C., Relvas, J.M.R.S., 2005. Transpressional tectonics, lower crust decoupling and intrusion of deep mafic sills: a model for the unusual metallogenesis of SW Iberia. Ore Geol. Rev. 27, 133–163.

Tornos, F., Solomon, M., Conde, C., Spiro, B.F., 2008. Formation of the Tharsis massive sulfide deposit, Iberian Pyrite Belt: geological, lithogeochemical, and stable isotope evidence for deposition in a brine pool. Econ. Geol. 103, 185–214.

Velasco, F., Sánchez-Espa, A.J., Boyce, A.J., Fallick, A.E., Sáez, R., Almodóvar, G.R., 1998. A new sulphur isotopic study of some Iberian Pyrite Belt deposits: evidence of a textural control on sulphur isotope composition. Mineral. Deposit. 34, 4–18.

Yuan, S.D., Peng, J.T., Hu, R.Z., Li, H.M., Shen, N.P., Zhang, D.L., 2008. A precise U-Pb age on cassiterite from the Xianghualing tin-polymetallic deposit (Hunan, South China). Mineral. Deposit. 43, 375–382.

Yuan, S.D., Peng, J.T., Hao, S., Li, H.M., Geng, J.Z., Zhang, D.L., 2011. In situ LA-MC-ICP-MS and ID-TIMS U-Pb geochronology of cassiterite in the giant Furong tin deposit, Hunan Province, South China: New Constraints on the timing of ti-polymetallic mineralization. Ore Geol. Rev. 43, 235–242.

Zhang, R.L., Lehmann, B., Seltmann, R., Sun, W.D., Li, C.Y., 2017. Cassiterite U-Pb geochronology constrains magmatic-hydrothermal evolution in complex evolved granite systems: the classic Erzgebirge tin province (Saxony and Bohemia). Geology 45, 1095–1098.

Zhu, Z.Y., Cook, N.J., Yang, T., Ciobanu, C.L., Zhao, K.D., Jiang, S.Y., 2016. Mapping of sulfur isotopes and trace elements in sulfides by LA-(MC)-ICP-MS: potential analytical problems, improvements and implications. Minerals 6. https://doi.org/10.3390/min6040110.